(2)

AD-A232 768

Annual Report

Analysis of Polarizing Optical Systems for Digital Optical Computing with Symmetric Self Electrooptic Devices

To:
Air Force Office of Scientific Research

From:
Department of Physics
The University of Alabama in Huntsville

Principle Investigator
Dr. Russell A. Chipman
205-895-6417

Investigators
J. Larry Pezzaniti
David B. Chenault

Contract # AFOSR-89-0542

November 16, 1990

REPORT DOCUMENTATION PAGE

Form Approved
OMB No. 0704-0188

1. AGENCY USE ONLY (Leave blank)	2. REPORT DATE	3. REPORT TYPE AND DATES COVERED
	16 Nov 90	30 Sep 89-30 Mar 91 Annual

4. TITLE AND SUBTITLE
Polarizing Optical Systems for Digital Optical Computing with Symmetric Self Electrooptic Devices

5. FUNDING NUMBERS
AFOSR-89-0542

6. AUTHOR(S)
Professor Russell Chipman

7. PERFORMING ORGANIZATION NAME(S) AND ADDRESS(ES)
Dept of Physics
Univ of Alabama in Huntsville
Huntsbille, AL 35899

AFOSR-TR. 91 0121

8. PERFORMING ORGANIZATION REPORT NUMBER

9. SPONSORING/MONITORING AGENCY NAME(S) AND ADDRESS(ES)
AFOSR/NE
Bldg 410
Bolling AFB DC 20332-6448
Dr Alan Craig

10. SPONSORING/MONITORING AGENCY REPORT NUMBER
2305/B1

11. SUPPLEMENTARY NOTES

12a. DISTRIBUTION/AVAILABILITY STATEMENT
UNLIMITED

12b. DISTRIBUTION CODE

13. ABSTRACT (Maximum 200 words)

Two architectural approaches have dominated the field of optical computing. The first approach uses integrated optics to connect logic gates in arbitrary configurations similar to a conventional computer. An optical computer built with this approach competes directly with a conventional computer. The approach is successful when it results in a computer which is more powerful and can be made more cheaply. The second approach makes use of 2-D arrays of logic devices itnerconnected in free space. This approach cannot provide arbitrary connections as do integrated optics but the density and the bandwidth of free space interconnects can be much larger than what is offered by conventional interconnects. A more fundamental advantage of optical interconnects is that lower energy communciations appear to be possible than with electronic interconnects.

14. SUBJECT TERMS

15. NUMBER OF PAGES

16. PRICE CODE

17. SECURITY CLASSIFICATION OF REPORT	18. SECURITY CLASSIFICATION OF THIS PAGE	19. SECURITY CLASSIFICATION OF ABSTRACT	20. LIMITATION OF ABSTRACT
UNCLASSIFIED	UNCLASS	UNCLASS	UL

Table of Contents

1. Introduction

Two architectural approaches have dominated the field of optical computing. The first approach uses integrated optics to connect logic gates in arbitrary configurations similar to a conventional computer. An optical computer built with this approach competes directly with a conventional computer. The approach is successful when it results in a computer which is more powerful and can be made more cheaply. The second approach makes use of 2-D arrays of logic devices interconnected in free space. This approach cannot provide arbitrary connections as do integrated optics but the density and the bandwidth of free space interconnects can be much larger than what is offered by conventional interconnects. A more fundamental advantage to optical interconnects is that lower energy communications appear to be possible than with electronic interconnects.[1]

Recently, SEEDs and related electrooptic devices have been proposed as potential components of free space digital optical computers because of their bistability, high speed, and low switching power.[2-5] SEEDs or self electrooptic effect devices exploit the quantum confined Stark effect in quantum well materials to produce optical bistability.[6,7] One version, the symmetric SEED or s-SEED, contains two SEEDs connected together across a fixed voltage, Figure 1 [8]. In this configuration, the s-SEED is optically bistable with two states, (1) SEED 1 is highly reflecting and SEED 2 is poorly reflecting, and (2) SEED 1 is poorly reflecting and SEED 2 is highly reflecting. The device has time sequential gain, such that the state of the device can be set with low power beams, and read out subsequently with high power beams. Because the device operates on the ratio of reflectances, it is insensitive to optical power supply fluctuations if both beams are derived from a single source. The s-SEED is especially promising for digital optical computing applications because it has good input/output isolation being time sequential. It does not require the critical biasing required of most bistable devices.

Spatial light modulators, optical dynamic memory[5], all-optical shift registers[9], and optical set-reset latches have been demonstrated using arrays of s-SEEDs[10]. Optical systems which compute or perform interconnections using arrays of SEEDs have been proposed and are under construction[11-12]. The focus of our studies have been on massively parallel optical processors constructed from interconnected or cascaded optical logic modules (COLM). This method of interconnection is based on the use polarizing elements and lenses. The polarization/lens based system allows efficient interconnections between devices at the cost of requiring regular interconnectivity.[11] These COLMs can be interconnected to form gates, adders, programmable logic arrays, and other components of conventional electronic computers. Figure 2 is a schematic of a single COLM. The section of the COLM shown separately in Figure 3, is used to clear the s-SEED array. The COLM reads out the SEED array, operates

on the information, and passes data to another COLM, where another SEED array is set. This system has been constructed at AT&T Bell Laboratories by M. Prise and operational details of this optical system are available in References 13,14.

The transmission efficiency or throughput of the COLM is limited, primarily, by two factors. First, it is limited by the quality of the polarizing beam splitters and waveplates used in its design, and second, by the alignment of the system. An imaging polarimeter has been assembled at UAH to align the polarizing elements in a COLM and to make comparative measurements COLM polarizing elements to decide which ones will work best. The goal of this research is to optimize the efficiency of a polarization based cascadable optical logic module of a digital optical computer.

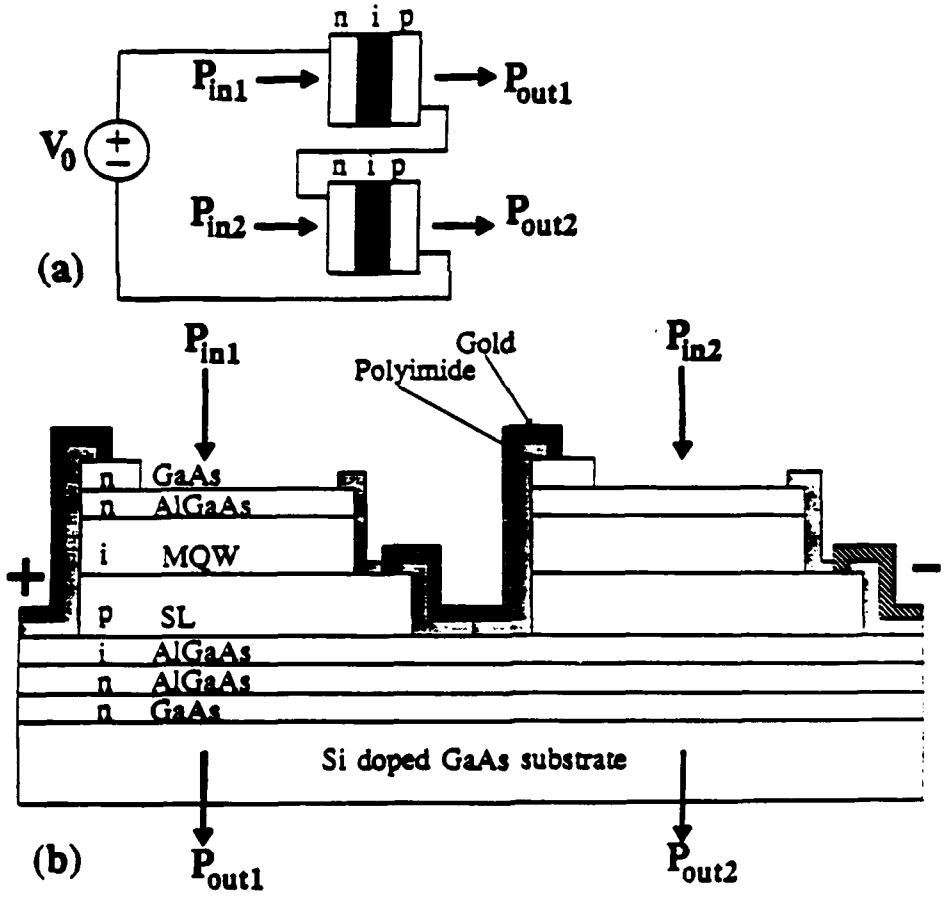

Figure 1 : Structure of symmetric self-electro-optic device.

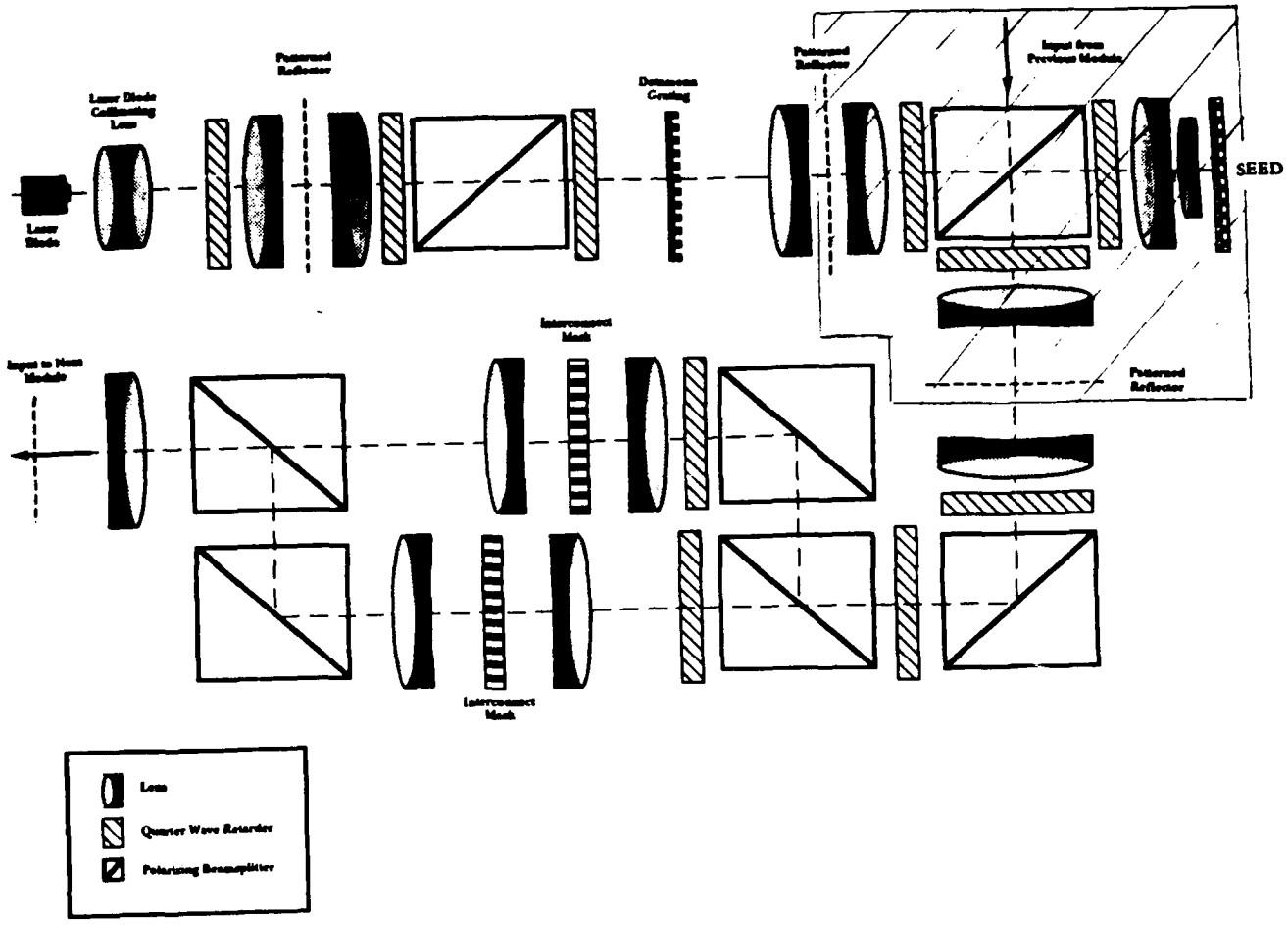

Figure 2 : Architecture of a cascadable optical logic device for a digital optical computer.

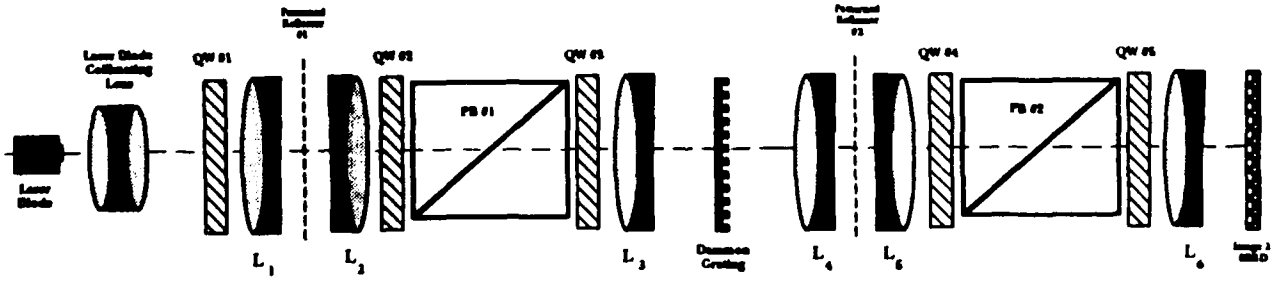

Figure 3 : Portion of the cascadable optical logic module that is used to clear the s-SEED.

Section 2 discusses the polarization aberration mechanisms of the polarizing elements used in the COLM. Included in this section is the analysis of the field angle dependence of a quarter wave plate and a polarizing beam splitter cube. Section 3 describes the Stokes imaging polarimeter. Section 4 describes the experimental configuration of the imaging polarimeter used to measure the field of view dependence of an achromatic polarizing beam splitter at 632.8 nm. The results of measurements made in transmission over a 10° field of view of a polarizing beam splitter cube are also presented in this section. Section 5 discusses the calibration issues associated with the imaging polarimeter that have been addressed and still need to be addressed. Section 6 describes a method of aligning the polarizing elements of a COLM using the imaging polarimeter. Finally in section 7 we provide some concluding remarks.

2. Background

2.1 Polarization beam combining

The heart of the COLM is the portion highlighted in Figure 1. This section of the COLM combines input beams from one logic module with the power beams of a second. The s-SEEDs are set by the input beams of the first logic module so that they can be read out by the power beams of the first. The method of combining beams from the two modules in this manner is called polarization beam combining.

Figure 4 shows a polarization beam combining system which allows four-port access to the s-SEED. From the left two signal beams in orthogonal linear polarization states reflect and pass through the polarizing beam splitter cube according to their polarization state. After passing through the quarter wave retarders, the beams are imaged onto the reflective portions of the patterned reflectors. The beams are thus transformed into left and right handed circular states and then reflected which inverts their handedness. Passing back through the wave plates converts their polarization back to linear so that the beams from mirror array 1 pass through the polarizing beam splitter and the beams from mirror array 2 reflect. Thus the signal inputs are imaged onto the s-SEED in orthogonal polarization states. The power beams are imaged between the mirror portions of mirror array 1 onto the s-SEED. The output power beams are reflected off the s-SEED, and the polarization is transformed again by the waveplate so that it reflects off the polarizing beam splitter and the beams exit the module through the spaces in mirror array 2.

Note that the patterned reflectors and s-SEED array are in image planes. This means that the system focuses the beams through the polarizing elements. Accordingly, rays up to approximately 10° pass through the polarizing elements. Therefore the behavior of the

polarizing elements over a 10 ° field of view must be determined. Furthermore, since a large cross-section of the polarizing elements are illuminated by the beams, the uniformity of the polarizing element is an issue that must be addressed.

The next two subsections in this section describe the field dependence of the polarizing elements used in the COLM. The last subsection analyzes the dependence of throughput of the COLM on the quality of the polarizing elements and alignment.

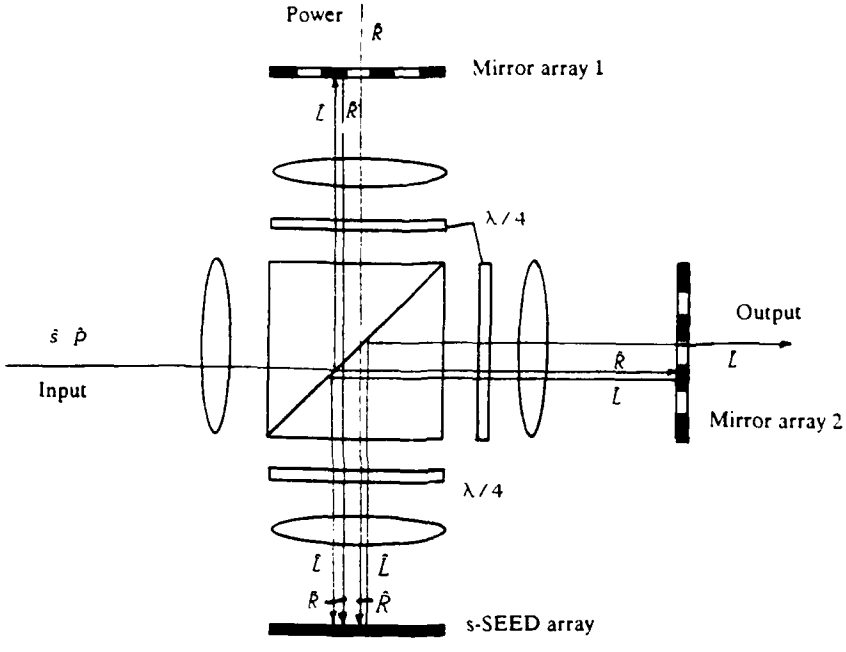

Figure 4 : Beam combining portion of the cascadable optical logic module.

2.2 Field of view effects of the polarizing beam splitters

A polarizing beam splitter cube's function is to split the incident $\hat{s}$ and $\hat{p}$ vibrations of an incident beam into perpendicular directions. That is, an ideal PBSC will transmit 100% p light and 0% s light; it will reflect 100% s light and 0% p light. Very good polarizers are obtained when the Banning condition[15] exists between the indices of the substrate and the thin films. Typically a polarizing beam splitter cube provides a large spectral range but a small angular range. Reference 16 researched the conditions necessary to spread out the angular field while keeping good polarizing characteristics. The authors design expanded the field of view but reduced the spectral range.

Based on the theory developed in the paper, the authors designed a polarizing beam splitter cube with a 5 degree field of view. We entered the design into Code V and traced rays using the polarization ray trace option to determine the cube's performance over a 10 degree field of view. The results are shown in Figures 5-6 as pupil intensity maps. The cube is situated with its multilayer plane of incidence vertical (the $\hat{x}$ axis). The positive $\hat{x}$ direction is the direction that light reflects. The central point corresponds to an axial ray, and the outermost points correspond to rays at a 10° angle of incidence.

Figure 5 is a pupil map of the polarizing beam splitter with converging 10° cone of incident light in p state of polarization (electric field oscillating in plane of incidence of multilayer). The numbers in the pupil map are the percent transmission of light that remains in the p polarization. The remaining light is either reflected or coupled into the orthogonal s state. Therefore the percentages seen in this pupil map correspond to the percentage of light that continues to propagate in the correct direction each time it encounters a polarizing beam splitter cube in the COLM.

Figure 6 is a pupil map similar to figure 1 only the incident polarization is in the s state and the behavior of the cube is observed in reflection. Again the percentages in the pupil map correspond to the percent of light that will continue to propagate in the correct direction.

The angular dependence of the polarizing beam splitter cubes used in the digital optical

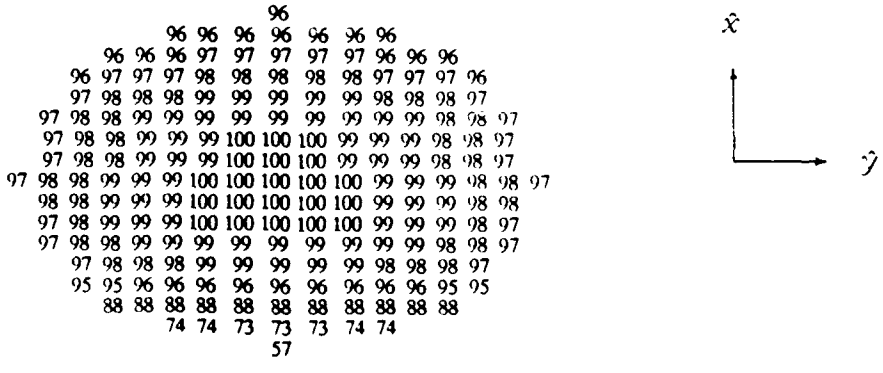

Figure 5 : Pupil map of a polarizing beam splitter cube created by ray trace performed using Code V ray trace software. A 10° half angle cone of converging light in the $\hat{p}$ state is incident. The map shows the percent transmitted light remaining in the $\hat{p}$ state.

computer greatly affect the efficiency and performance of this architectural approach to digital optical computing. The measurements made with the imaging polarimeter correspond directly to the above ray trace study. The measurements made with the imaging polarimeter on a number of polarizing beam splitter cubes will tell us which cube design has the best angular behavior and uniformity.

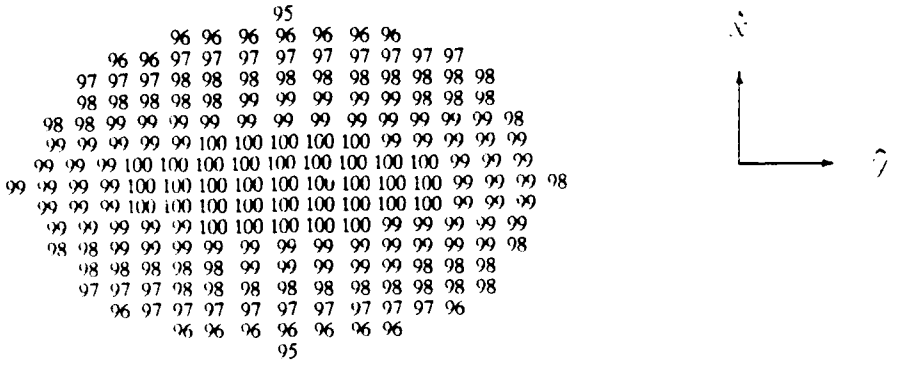

Figure 6 : Pupil map of a polarizing beam splitter cube created by ray trace performed using Code V ray trace software. A 10° half angle cone of converging light in the $\hat{s}$ state is incident. The map shows the percent reflected light remaining in the $\hat{s}$ state.

2.2 Field of view effects of the retarders

Several characteristics of birefringent retarders introduce polarization aberration in polarization critical systems. First, the thickness of the birefringent material may be wrong or wedged, yielding an incorrect or spatially varying retardance. The crystal axis can be misoriented relative to the faces or the mount. The retarder can be misaligned in the optical system, either tilted or with its fast axis at the wrong orientation.

Three other problems with retarders are more fundamental, angular field dependence, diattenuation, and birefraction.

The angular dependence of a uniaxial crystal is illustrated in Fig. 7. For a crystal axis in this orientation, two conflicting effects are present. First, the difference between the extraordinary and ordinary refractive index, or birefringence, decreases quadratically with increasing field angle. Therefore the optical path length will also decrease. The second effect tends to offset the first effect somewhat. This effect is simply due to the increase in physical path length with angle.

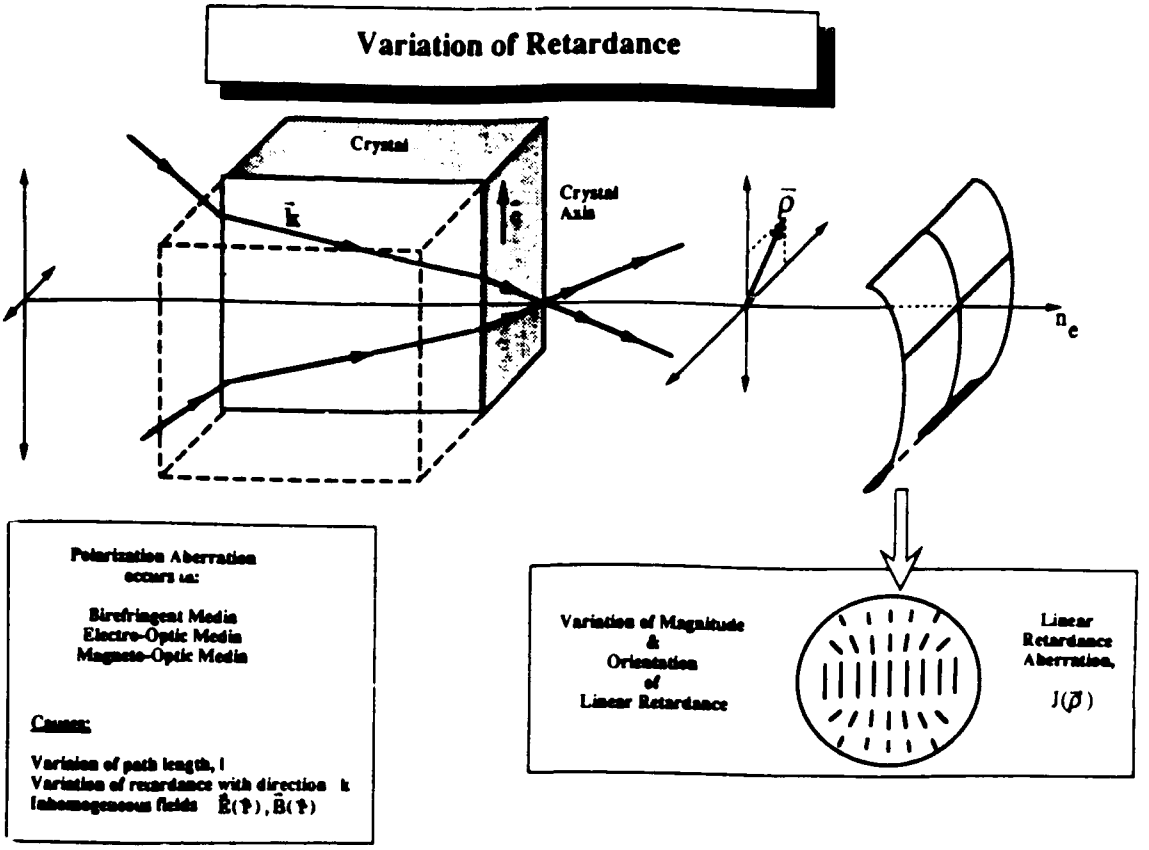

Figure 7 : Illustrates the angular dependence of birefringence in a uniaxial crystal. From the index ellipsoid we see a quadratic variation in birefringence with ray angle.

Figure 8 shows variation in retardance with field angle in quartz crystal. The numbers shown are normalized to a quarter wave of retardance. The crystal axis is along the $\hat{y}$ axis and linear polarization at 45 degrees with respect to the $\hat{y}$ axis is incident. Shown is one quadrant with the lower left corresponding to an axial ray and the angle of incidence increasing along the $\hat{x}$ and $\hat{y}$ axes. By symmetry, it is only necessary to view the angular dependence in one quadrant. For an ideal quarter wave retarder, about a 1% variation of retardance is found over a 10 degree field of view.

Figure 9 shows double refraction in birefringent uniaxial media. The crystal axis is represented by $\vec{c}$. When the propagation vector is not parallel to the crystal axis or normal to the interface, the extraordinary and ordinary beams will shear apart as shown. The desired polarization will only be where the two sheared beams overlap in the center. The two crescent shaped portions of the beam are the portions that do not overlap, but remain in their original states (their eigenpolarization states).

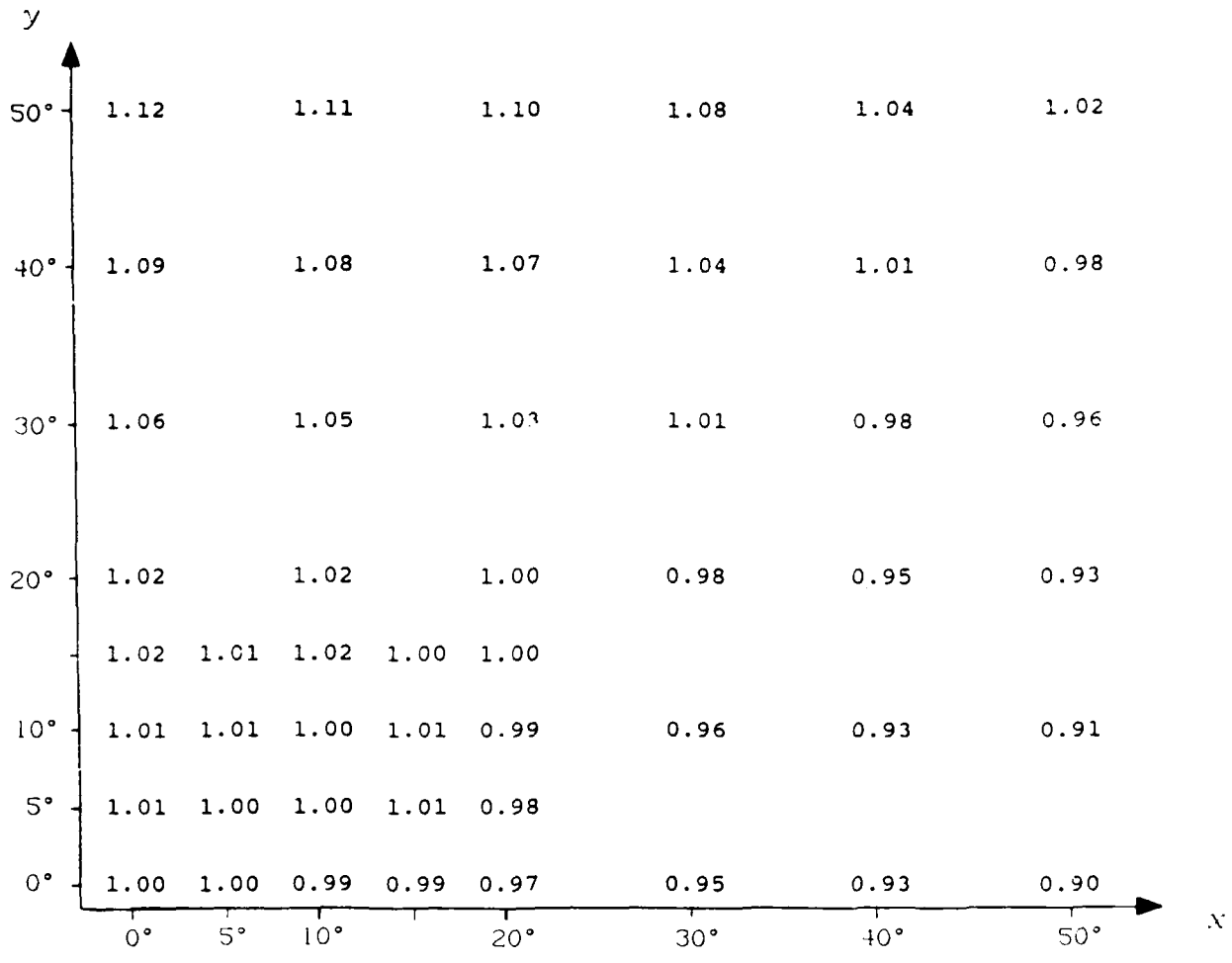

Figure 8 : Illustrates the variation in retardance of a quartz quarter wave retarder with ray angle. The Numbers shown have been normalized to a quarter wave of retardance.

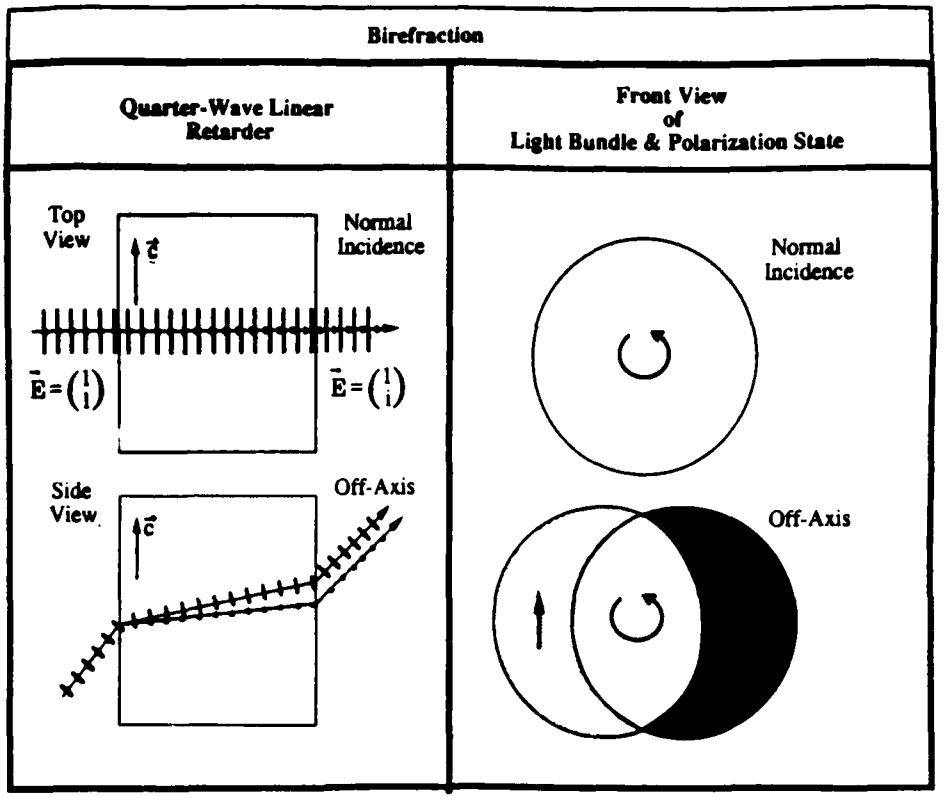

Figure 9 : Shows double refraction and beam shear in a uniaxial crystal.

The imaging polarimeter is a useful tool for studying the angular dependence of birefringent devices and the uniformity, or lack of uniformity. Again, the imaging polarimeter will be used to take data on many quarter wave plates to determine which ones are best suited for the digital optical computer.

2.3 Performance of an entire COLM

The imaging polarimeter will be used to study polarization aberration of an entire COLM. One issue this particular study will address is the polarization aberration and loss of throughput due to misalignment and azimuthal orientation errors of the polarizing elements. An analytical study has been done to determine the sensitivity of COLM throughput to misorientation of the quarter wave retarders. Figure 10 shows the percent transmission of light that remains in the correct polarization state as a function of orientation error of the quarter wave retarders. Each retarder received the same amount of orientation error. The percent transmission refers to the percentage of light emitted from the laser diodes that travels through the entire COLM to the next COLM. The quarter wave plates and polarizing beam splitter cubes were assumed ideal. The imaging polarimeter will be used to tweak the orientation alignment of the quarter wave plates to obtain maximum throughput (see section 6).

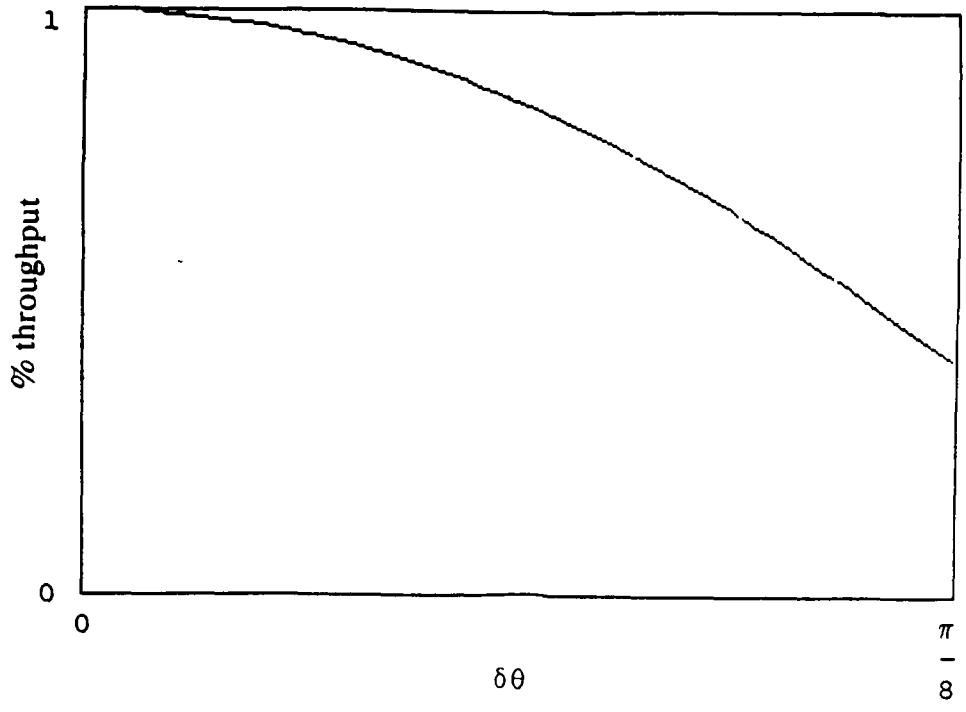

Figure 10 : Plot of percent throughput as a function of orientation error of the quarter wave retarders. Each quarter wave retarder received the same amount of orientation error.

Figure 11 shows the relationship between the polarizing beam splitter cubes' transmission coefficients and throughput of a COLM. For this analysis, each of the polarizing beam splitters are assumed to behave ideal in reflection and have the same transmission coefficient. Each beam that propagates through the COLM will see slightly different transmission coefficients at the beam splitter cubes and therefore each beam will have an unique associated overall transmission coefficient. Figure 12 shows a similar plot of throughput, except the reflection coefficients of the polarizing beam splitter cubes vary and the transmission coefficients are assumed to be ideal. Note that COLM throughput is more sensitive to variation of reflection coefficients of the beam splitter cubes from ideal behavior than transmission variation.

The imaging polarimeter will eventually be used to calculate the spatial dependent Mueller matrix of the COLM. This Mueller matrix will represent all of the above described polarization aberration mechanisms. In this regard it will completely characterize the polarization behavior of the cascadable optical logic module.

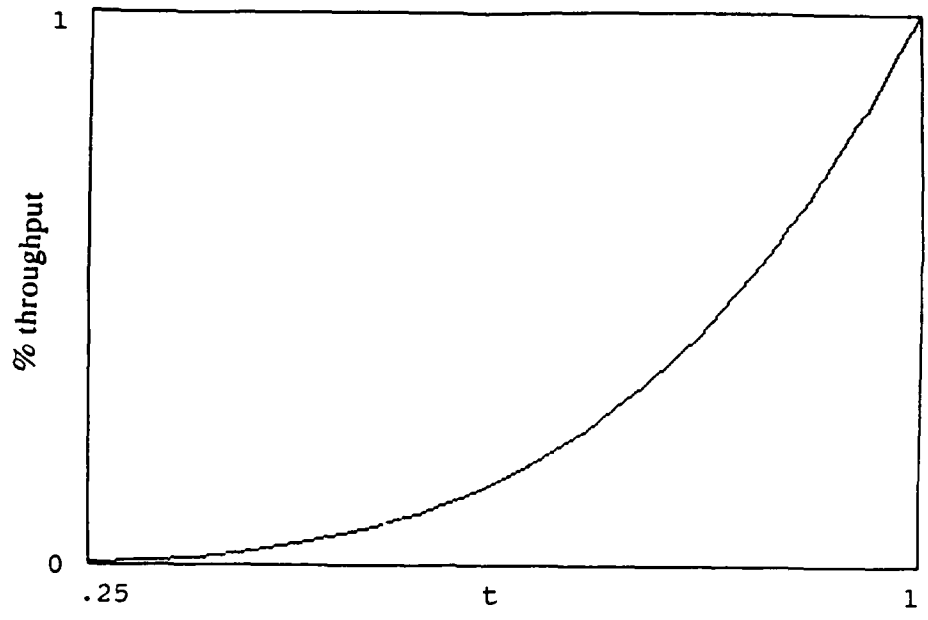

Figure 11 : Plot of percent throughput as a function of transmission coefficient of the polarizing beam splitter cubes. Each polarizing beam splitter cube received the same transmission coefficient and ideal reinfection was assumed.

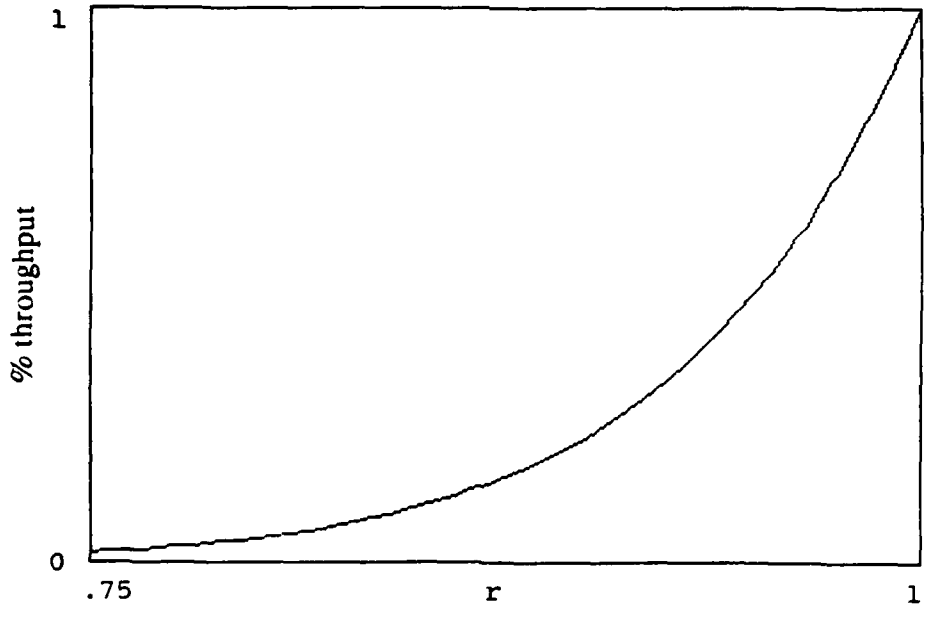

Figure 12 : Plot of percent throughput as a function of reflection coefficient of the polarizing beam splitter cubes. Each polarizing beam splitter cube received the same reflection coefficient and ideal transmission is assumed.

3. Stokes imaging polarimeter

The UAH Stokes imaging polarimeter was assembled primarily for polarimetric metrology of optical systems[21]. We operate the Stokes imaging polarimeter by introducing a plane wave or spherical wave of known polarization state to the optical element or optical system under test, and measure Stokes images of the transmitted light. We thus characterize the polarimetric response of the optical system to a waveform of known polarization. Section 4 describes the Mueller matrix imaging polarimeter which characterizes the system for any arbitrary incident polarization state. A brief review of Mueller/Stokes calculus is at the beginning of section 4.

The Stokes images are generally measured at either the exit pupil or image plane by focusing the camera on that plane. For instance when the camera is focused on the exit pupil, each pixel of the camera corresponds to a ray path through the optical system under test and the imaging polarimeter measures the polarization aberration function[17,18]. If the camera is focused on the image plane, then the distribution of polarization states in the point spread function is measured and the polarization point spread function of the system is determined in Stokes vector form. Since the point spread function is usually only a few microns in diameter, a microscope objective or other high magnification system is needed to observe the structure of the point spread function with the ccd camera.

A schematic of the UAH Stokes polarimeter is shown in Figure 13. The polarimeter consists of a rotating quarter wave retarder in front of a fixed polarizer. Currently, the Stokes imaging polarimeter works by capturing four images at four different orientations of the quarter wave retarder and using these intensity modulated images solves for the four Stokes parameters of the incident light on a pixel by pixel basis. Details about the hardware and camera used is given in section 4.4.

Another version of the Stokes imaging polarimeter that has been developed uses a rotating polarizer in front of the ccd camera. This polarimeter only gives the first three stokes parameters: s_0, s_1, s_2.

The s_1, s_2, s_3 Stokes images can be normalized by the image intensity s_0 to produce images with only polarization information. For instance normalized s_3 is the fraction of circular polarization in the wavefront, or the degree of circular polarization (DOCP). DOCP is zero for completely linear or unpolarized light and one for right circular polarized light, negative one for left.

Other useful measures that can currently be displayed as images include:
the degree of polarization DOP

$$\mathrm{DOP} = \sqrt{\frac{s_1^2 + s_2^2 + s_3^2}{s_0}}. \qquad (1)$$

DOP varies from zero for unpolarized light to one for polarized light.

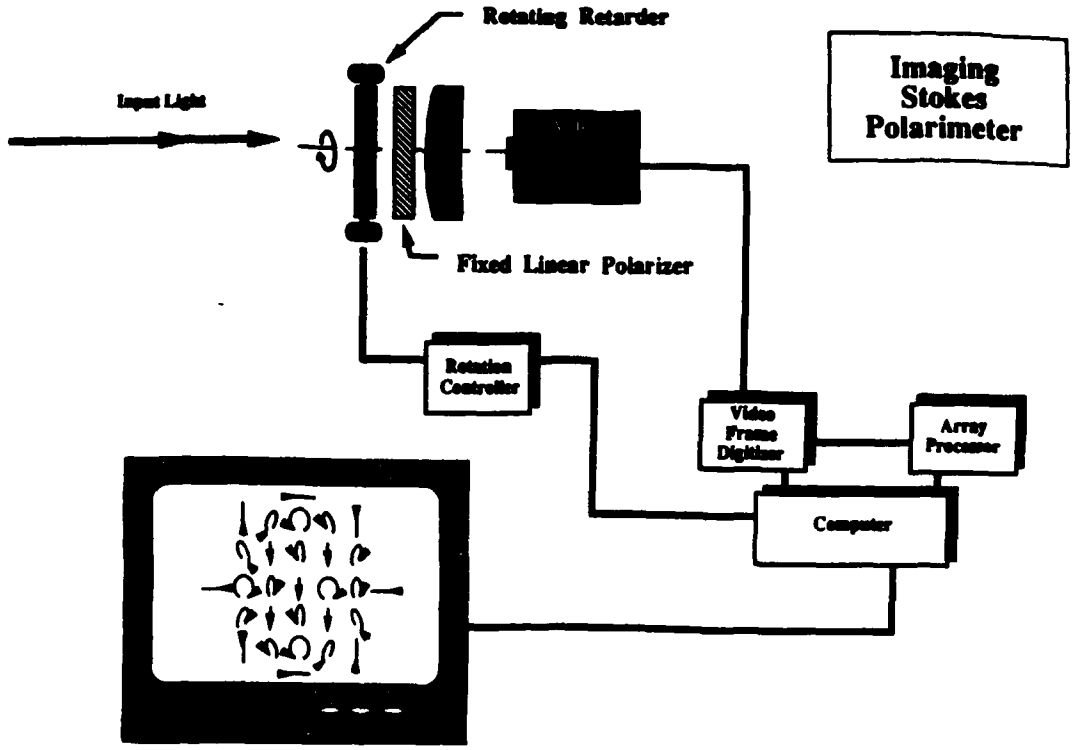

Figure 13 : Schematic diagram of UAH Stokes Imaging Polarimeter.

The degree of linear polarization DOLP is a measure of the amount of linear polarization

$$\mathrm{DOLP} = \sqrt{\frac{s_1^2 + s_2^2}{s_0}}. \tag{2}$$

DOLP is zero for unpolarized or circularly polarized light and one for polarized light.

Two other definitions specify a polarization ellipse. The eccentricity χ of the polarization ellipse is

$$\chi = \frac{1}{2} arcsin\left(\frac{s_3^2}{s_1^2 + s_2^2 + s_3^2}\right), \tag{3}$$

and the orientation α of the major axis of the polarization ellipse is

$$\alpha = \frac{1}{2} arctan\left(\frac{s_2}{s_1}\right). \tag{4}$$

The orientation and eccentricity can be used to display graphical maps of polarization aberration which may contain arrays of polarization ellipses representing the average polarization of regions of the wavefront, such as is shown in Figure 14.

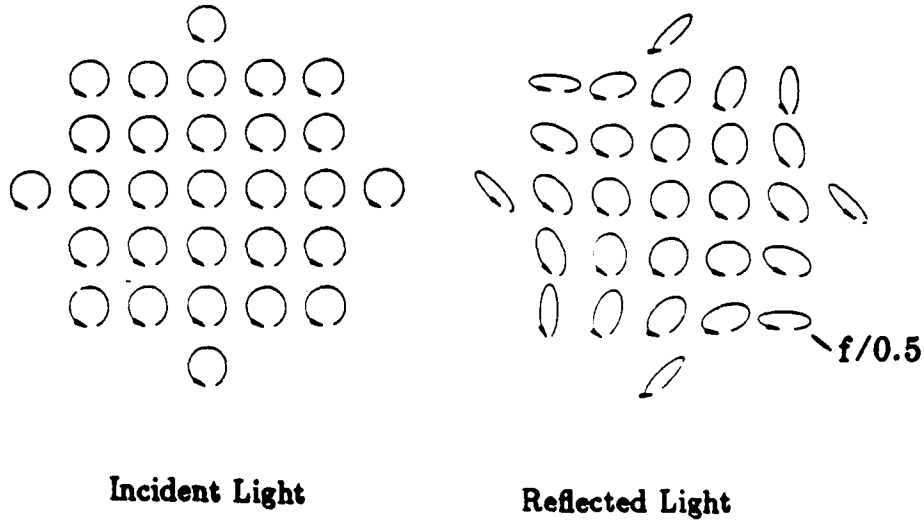

Figure 14 : The effect of a f/0.5 telescope mirror on circularly polarized light. Elliptical polarization around the edge is due to tangentially oriented linear retardance of the interface.

Code to calculate all four Stokes images using the rotating retarder scheme has been developed. Code has also been developed to calculate the first three Stokes images using the rotating polarizer scheme. Each of the above algorithms calculate the associated normalized Stokes images as well. A program has also been written to calculate DOP, DOLP, DOCP, and the eccentricity and orientation of polarization ellipse from the normalized Stokes images. Code to produce graphical maps of polarization ellipses from the normalized Stokes parameters has not been written yet.

Calibration issues that have been addressed and those that need to be addressed are covered in section 5.

4. Mueller matrix imaging polarimeter

This section describes the Mueller matrix imaging polarimeter. After a brief summary of Mueller matrix formalism, we describe the system design used to measure field of view dependence of a polarizing beam splitter cube. Following this is a presentation of the results of measurements made on an achromatic polarizing beam splitter cube at 632.8 nm.

4.1 Mueller Matrix Formalism

The Mueller matrix formalism is based upon the representation of the state of polarized light by a 4 X 1 real Stokes vector. The Mueller matrix is a 4x4 real matrix which maps an input polarization state into an output polarization state. We are interested in measuring the

Mueller matrix for rays between conjugate planes in an optical system; in particular between object-image planes and pupil planes. Each ray path through the optical system will have slightly different polarizing effects because of variations in the angles of incidence at interfaces (thin films interfaces) and because of different path lengths through birefringent and dichroic materials. The ray path dependence of the Mueller matrix of an optical system can be written as a function of object coordinate $\bar{h}$, pupil coordinate $\bar{\rho}$ and wavelength λ [17-18]. The spatial dependence of the Mueller matrix gives rise to polarization aberrations at the exit pupil of the optical system[17-20]. The Mueller matrix imaging polarimeter measures the spatial dependence of the Mueller matrix for a set of ray paths through an optical system.

Typically we are interested in measuring specific parts of the Mueller matrix which are important to determine the polarizing characteristics of a particular polarizing element. For example, in the next section we describe the procedure used to measure a 2x2 sub-matrix of the Mueller matrix of a polarizing beam splitter cube. Measurement of this sub-matrix is an important diagnostic for polarizing beam splitters that will go into a cascadable logic module.

4.2 System design of the Mueller matrix imaging polarimeter for measuring polarizing beam splitter cubes

The block diagram in Figure 15 shows the basic design of the imaging polarimeter used to measure the polarizing beam splitter. The light source is a polarized 632.8 nm wavelength He-Ne laser. The beam is focused to a 100 micron spot onto a rotating ground glass disk, thereby reducing diffraction and interference effects in the image at the ccd caused by dust or imperfections on the optics. The beam is then collimated and passed through a Glan-Thompson polarizer and an achromatic half wave retarder both placed in manual high resolution rotation stages. The polarizer/HWP pair comprises the polarization generator. The collimated light is then expanded to a 10° half angle cone of light. The divergent light then passes through the polarizing beam splitter cube. The last surface of the cube is the stop of the system. The beam is then reduced and collimated to pass through the rotating polarizer. The exit pupil which is image of the last surface of the PBSC is magnified and imaged onto the ccd.

To control system operation, capture and process images, and display the results, a PC 386 computer with the following peripherals is used. A 512 X 512 video frame grabber board with 8-bit resolution in conjunction with a visible/near infrared monochrome ccd camera. A multisync color monitor is used to display false colored measured frames and calculated false color pupil maps of the polarizing beam splitter. Measured frames are shipped over the PC bus to PC memory where high precision floating point processing is performed.

Each measured frame is divided into 4 X 4 pixel squares which we will call bixels. The value of the bixel is the average value of the 4 X 4 square. As the bixel size is increased the angular resolution of the measurement is decreased.

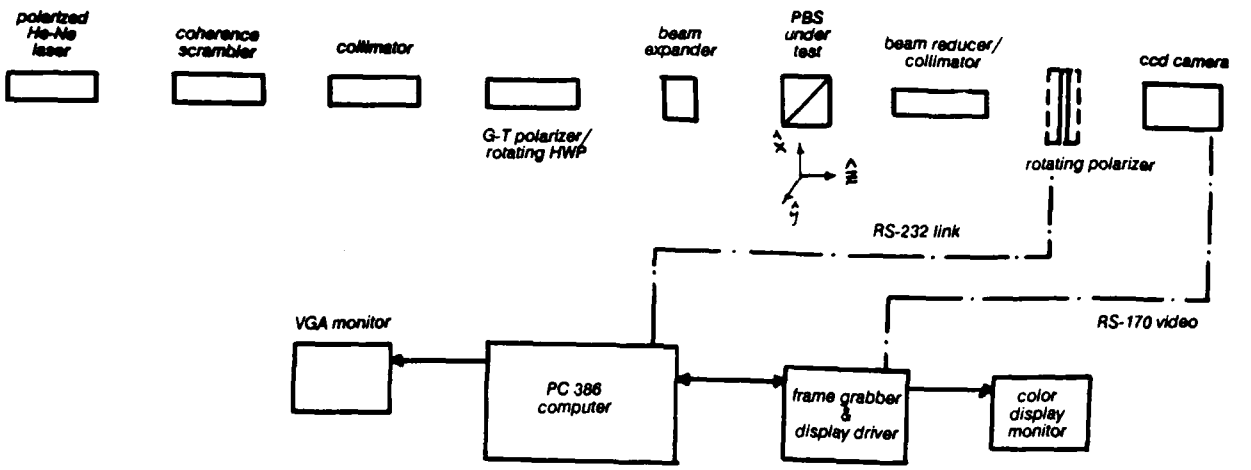

Figure 15 : Schematic diagram of Imaging Polarimeter used to measure the polarizing properties of a polarizing beam splitter cube.

Bixels are used to provide a spatial integration of the intensity variation due to speckle on the ccd. Using bixels also decreases the effect of beam wander due to element wedge in the rotating polarization elements (see section 5.5). The trade off is a decrease in resolution. For measurements of the polarizing beam splitter, high resolution is not important since field of view dependence of PBSC is slowly varying.

4.3 Measurement of PBSC

The imaging polarimeter, in this configuration, measures the performance of the polarizing beam splitter cube for several meridinal and skew rays. By sending in spherical waves of known polarization and analyzing the light with the polarizer/ccd camera combination (the Stokes polarimeter), the following performance parameters are measured. Transmission throughput is measured when linearly polarized $\hat{p}$ light is incident and the transmission axis of the polarization analyzer is parallel to $\hat{p}$ direction. Transmission leakage is measured when $\hat{s}$ light is incident and the total amount of light transmitted is measured. Couplance is measured when $\hat{p}$ is incident and the amount of transmitted $\hat{s}$ light is measured. Transmission throughput and leakage can also be measured for incident unpolarized light. The same performance measurements are made in reflection except $\hat{s}$ light is sent in place of $\hat{p}$ and $\hat{p}$ light in place of $\hat{s}$.

Each of these measurements were made with a 10° half angle cone of incident light. The results are shown as pupil maps, similar to the ones generated by ray tracing in section 2.2, and are given in Figures 16-18. The $\hat{x}$ axis is in the plane of incidence of the multi-layer of the PBSC for an axial ray. The positive $\hat{x}$ direction is the direction light reflects when facing the back surface of the PBSC (compare coordinates in Figures 15 & 16-18). Each color square in the pupil map is a bixel corresponding to a definite solid angle bundle of rays propagating

through the PBSC.

Figure 16 is a false color plot of the transmission throughput of a polarizing beam splitter cube as a function of ray angle. The center of the pupil map corresponds to an axial ray and the edge represents rays that subtend a 10 degree angle to the optical axis. The transmission throughput is symmetric about the $\hat{y}$ axis as expected. However the throughput falls off faster in the negative $\hat{x}$ direction than the positive direction. This behavior is consistent with what was found by tracing rays through a modified Macneille polarizing beam splitter cube (see Figure 5). In this plot an overall variation in throughput of 50% is observed with a resolution of better than 10%.

Figure 17 is a plot of transmission leakage as a function of ray angle. The leakage is below a half percent for axial rays and rays within the plane of incidence in the negative $\hat{x}$ direction. The leakage of $\hat{s}$ light increases for non-axial rays in other directions up to about 1.5% to 2.0%.

Figure 18 is a plot of the couplance of incident $\hat{p}$ light into transmitted $\hat{s}$ light. For rays along the plane of incidence of the polarizing beam splitter cube no couplance is observed. The incident polarization is an eigenstate of the cube in this plane. Rays in other directions couple more strongly into the orthogonal polarization for two reasons. First, a coordinate rotation of the polarization direction takes place for skew rays at the multi-layer interface. That is, the electric field vibration incident on the multilayer must be decomposed into $\hat{p}$ and $\hat{s}$ states for non-meridinal rays. The second coupling mechanism is due to the slight birefringence of the multilayer.

The next measurements to be done will be made at 850 nm to supply AT&T Bell Labs with comparative data on polarizing beam splitter cubes needed in the optical computer.

5. Calibration Issues

In this section, the issues of camera calibration, bootstrap calibration of the polarization generator and analyzer elements, movement in the scene, source/detection fluctuations, beam wander, and instrumental polarization are discussed.

5.1 Camera calibration

Camera calibration can be relaxed somewhat due to the nature of our measurement technique. Our calculated images, or pupil maps in the case of the PBSC measurements, consist of added and surfaced images divided by another image. Normally each pixel grey value would need to multiplied by a sensitivity factor which is slightly different for each pixel (sometimes 10%), but since our images ratioed, the sensitivity factor drops out. However, the dark count (pixel value at zero light level) must be subtracted out of each measurement.

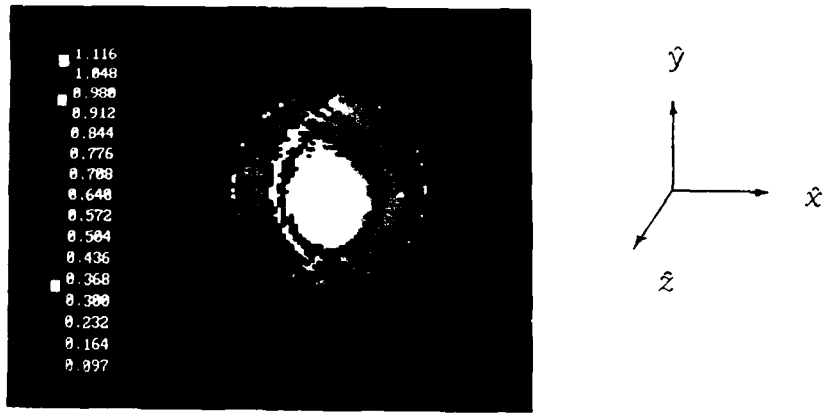

Figure 16 : Transmission throughput as a function of ray angle of a polarizing beam splitter cube. Measured with the UAH imaging polarimeter at 632.8 nm.

Figure 17 : Transmission leakage as a function of ray angle of a polarizing beam splitter cube. Measured with the UAH imaging polarimeter at 632.8 nm.

Figure 18 : Couplance of $\hat{p}$ into $\hat{s}$ as a function of ray angle of a polarizing beam splitter cube. Measured with the UAH imaging polarimeter.

Each of the data reduction algorithms mentioned in sections 3 and 4 presently do this.

If Fourier methods are used, which do not involve division of images, a sensitivity file containing information about the gain of each pixel must be formed. Each measured image would be multiplied by the sensitivity file to compensate for pixel gain variation of the ccd.

5.2 Polarizing element calibration

Without sufficient prior knowledge of the properties of the polarization elements, a bootstrap calibration needs to performed, i.e. a calibration using retarders and polarizers with unknown properties. The calibration should make the fewest number of assumptions about the polarizing elements and utilize methods that are relatively insensitive to the weakest assumptions. Once an accurate Mueller matrix polarimeter is operating, it can be used to calibrate polarization elements for other polarimeters, greatly simplifying the exacting task of construction and accurate imaging polarimeter.

Preliminary calibration has been done on the UAH imaging Stokes polarimeter. Polarizer calibration assumed that the polarizers only display diattenuation. The transmittance of the transmission axis and the absorption axis of polarizers were measured. Two similar polarizers were calibrated in this way were then used to calibrate the retarders. The first nine elements m_{11} through m_{33} of the retarder Mueller matrix were measured by rotating the polarizers at a 3:1 ratio on either side of the quarter wave retarder. The resulting intensity modulation has four harmonics and a dc term in its Fourier series which will solve for the nine Mueller matrix elements. The linear retardance and linear diattenuation can be obtained from these nine Mueller matrix components assuming there is no circular retardance. Circular retardance occurs in multiple element linear retarders when the fast axes of the linearly birefringent elements are not exactly 0° or 90° apart. To test for circular retardance, the QWLR was placed between two crossed linear polarizers with its fast parallel to the transmission axis of the first polarizer. If circular retardance is present, the electric field vector is rotated slightly, so that the final polarizer must be rotated to locate the null. No circular retardance was observed in these retarders, but we have detected it in other linear retarders. If circular retardance is observed, the remaining seven components of the QWLR Mueller matrix should be measured. A method to measure these components is described in reference 22.

5.3 Speed of data acquisition

The imaging polarimeters discussed here take measurements sequentially in time and are sensitive to drift. Any change in source intensity or any drift in camera sensitivity during the measurement sequence is a source of 1/f noise. The measurements must be made as quickly as mechanically possible. The rotation stage which rotates the polarization generating and analyzing elements is the limiting factor. Ideally the stage should rotate the polarizing element into position during one frame period or 1/30th second. This would be a dead frame period. In the case of the Stokes polarimeter, if frame averaging is not done, the measurement time required would be four frames for data acquisition and three dead frames, or 7/30th of a second. High speed data acquisition may enable polarimetric measurements of quasi-still life such as planes, boats or vegetation.

5.4 Beam wander

Another important calibration issue is beam wander. To understand the problem, consider how digital image processors calculate derivatives. A partial derivative of the image intensity in the x direction is calculated by shifting the image in the x direction and subtracting the image from itself. The imaging polarimeter performs data reduction by adding and subtracting images. A moving object in the scene introduces spurious contributions into the Stokes images proportional to the resulting intensity derivatives. These intensity gradients are often greatest around the objects edges, but edges are where many objects have their greatest polarization signatures. Fortunately, in optical system polarimetric metrology, our subject is usually a fixed optical system and the intensity gradients are generally small. Thus, far more accurate polarimetry is possible in this setting than in remote sensing or tactical polarimetry.

The faces of QWLR need to be highly parallel because wedge in a rotating element generates beam wander. If the retarder is slightly prismatic, the image will move in a circle on the ccd resulting in a spatial misregistration and image derivatives. Large amounts of beam wander can be partially compensated by carefully shifting the measured images in software.

5.5 Instrumental polarization

The instrumental polarization due to wavefront shaping optics within the polarimeter may require compensation during data reduction. Their instrumental polarization will have to be determined each time a new optical system is configured within the sample compartment, so standardized methods for removing this systematic error should be developed.

6. Alignment of a logic module using the imaging polarimeter

Careful alignment of the logic modules must be performed so that the spots hit the correct places on the patterned reflectors and the s-SEEDs. Furthermore, the azimuthal orientation of the waveplates must be adjusted to insure that the system is operating with the greatest possible throughput. The imaging polarimeter can be used to maximize the amount of light that is in the correct polarization state at each stage of the COLM. The procedure, in short, is to aim the imaging polarimeter into a certain stage of the COLM such that the camera is focused onto a pupil. Next, set the polarization analyzer orthogonal to the expected state of polarization transmitted from that part of the stage. Finally, make slight azimuthal adjustments on the quarter wave retarders until optimal extinction is observed over the entire pupil. This maximizes the amount of light that is in the correct polarization state. By doing this at each stage of the logic module, the entire system can be tweaked to arrive at the maximum output.

7. Conclusions

The performance of a cascadable logic module depends heavily on the quality of the polarizing elements and their alignment. A imaging polarimeter has been constructed to measure the uniformity and angular dependence of the polarizing beam splitter cubes and the waveplates to generate a data base on the polarizing elements in order to determine which ones (which manufacturer) are best suited for the system. The imaging polarimeter will also be used to align and to understand the propagation of polarized light in such systems with large numbers of polarizing beam splitters and retarders.

Presently software has been written for the rotating retarder polarimeter, the rotating polarizer polarimeter, the polarizing beam splitter measurements, and to calculate the first nine elements (m_{11} thru m_{33}) of the Mueller matrix. Software to display the output from each of the above systems in false color has been developed.

Measurements of the angular behavior of a polarizing beam splitter cube have been made. Measurements on other polarizing beam splitter cubes will be made using the present method in order to form a database of comparative data on many polarizing beam splitter cubes.

The imaging polarimeter will be used to align a cascadable logic module and determine what alignment tolerances must be maintained for optimal efficiency.

7. References

1. A. Huange, "Architectural considerations involved in the design of an optical digital computer," Proc. IEEE **72**, 780-786 (1984).

2. D.A.B. Miller, D.S. Chemla, T.C. Damen, A.C. Gossard, W. Wiegmann, T.H. Wood and C.A. Burrus, "Novel hybrid optically bistable switch: The quantum well self-elector-optic effect device," Appl. Phys. Lett. **45**, 13 (1984).

3. D.A.B. Miller, D.S. Chemla, T.C. Damen, T.H. Wood, C.A. Burrus, A.C. Gossard and W. Wiegmann, "The quantum well self-electro-optic-effect device ,optoelectronic bistability and oscillation, and self linearized modulation," IEEE J. Quantum Electron, **QE-21**,1462 (1985).

4. D.A.B. Miller, J.E. Henry, A.C. Gossard, and J.H. English, "Integrated quantum well self-electro-optic effect device: 2x2 array of optically bistable switches," Appl. Phys. Lett. **49**, 821 (1986).

5. G. Livescu, D.A.B. Miller, J.E. Henry, A.C. Gossard, and J.H. English, "Spatial light modulator and optical dynamic memory using integrated symmetric self-electro-optic effect devices," in *Postdeadline Papers, Conference on Lasers and Electro-optics* (Optical Society of America, Washington DC 1987), paper ThU11; Optics Lett., April 1988.

6. D.A.B. Miller, D.S. Chemla, T.C. Damen, A.C. Gossard, W. Wiegmann, T.H. Wood and C.A. Burrus, "Band-edge electroabsorption in quantum well structures: The quantum confined stark effect," Phys. Rev. Lett. **53**, 2173 (1984).

7. D.A.B. Miller, D.S. Chemla, T.C. Damen, A.C. Gossard, W. Wiegmann, T.H. Wood and C.A. Burrus, "Electric field dependence of optical absorption near the band gap of quantum well structures, "Phys. Rev. B **32**, 1043 (1985).

8. A.L. Lentine, H.S. Hinton, D.A.B. Miller, J.E. Henry, J.E. Cunningham, and L.M.F. Chirovsky, "Symmetric self-electro-optic effect device:Optical set-reset latch,"Appl. Phys. Lett., **52**, 1419 (1988).

9. F.B. McCormick, A.L. Lentine, L.M.F. Chirovsky, and L.A. D'Asaro, "An all-optical register using symmetric self electro-optic effect devices," in Conference on Photonic Switching (Optical Society of America, Salt Lake City, Utah, 1989), paper ThC5-1.

10. A.L. Lentine, H.S. Hinton, D.A.B. Miller, J.E. Henry, J.E. Cunningham, and L.M.F. Chirovskiy, "Symmetric self-elctro-optic effect device: Optical set-reset latch," Appl. Phys. Lett., **52**, 1419(1988).

11. M.E. Prise, N. Striebl, and M.M. Downs, "Optical considerations in the design of a digital optical computer," Optical and Quantum Electronics, **20**, 49-77, 1988.

12. M.E. Prise, M.M. Downs, F.B. McCormick, S.J. Walker, and N. Streibl, "Design of an optical digital computer," OSA Topical Meeting on Optical Bistability, OB-4 (March 1989).

13. M.E. Prise, N.C. Craft, R.E. LaMa-.he, M.M. Downs, S.J. Walker, L.A. D'Asaro, and L.M.F. Chirovsky, "Module tor optical logic circuits using symmetric self-electrooptic effect devices," Appl. Optics **29**, 2164-2170 (1990).

14. A. Dickenson and Michael E. Prise, "Free-space optical interconnection scheme," Appl. Optics 29, 20012005 (1990).

15. M. Banning, "Practical methods of making and using multilayer filters," J. Opt. Soc. Am. **37**, 792-797 (1947).

16. J. Mouchart, J. Begel and E. Duda, "Modified MacNeille cube polarizer for a wide angular field," Appl. Optics 28, 2847-2853 (1989).

17. R.A. Chipman, "Polarization analysis of optical systems," Opt. Eng. **28**, 90-999 (1989).

18. R.A. Chipman, "Polarization analysis of optical systems II," Proc. SPIE **1166**, 79-94 (1989).

19. J.P. McGuire, Jr. amd R.A. Chipman, "Polarization aberrations in optical systems," Current Developments in Optical Engineering II, R. Fischer, W.Smith, Editors, Proc. SPIE **81**, 240 (1987).

20. R.A. Chipman and L.J. Chipman, "Polarization aberration diagrams," Opt. Eng. **28**, 100-106 (1989).

21. J.L. Pezzaniti and Russell A. Chipman, "Imaging Polarimeters for optical system metrology," Proc. SPIE **1317**, 280-294 (1990).

22. M.F. Morgan and R.A. Chipman, "An ultraviolet polarimeter for characterization of an imaging spectrometer," Proc. SPIE **1317**,384-394 (1990).